

Lasers in Manufacturing Conference 2017

## Characterization and optimization of residual stress state, geometrical accuracy and productivity for laser metal deposition of complex three-dimensional titanium parts

Mauritz Möller<sup>a,\*</sup>, Christoph Scholl<sup>b</sup>, Vishnuu Prakash<sup>b</sup>, Claus Emmelmann<sup>b</sup>

<sup>a</sup>Bionic Production GmbH, Am Schleusengraben 14, D-21029 Hamburg

<sup>b</sup>Institute of Laser and System Technologies, Hamburg University of Technology, Denickestraße 17, D-21073 Hamburg

---

### Abstract

Laser Metal Deposition (LMD) connected with milling processes offers the opportunity for an efficient, resource conserving manufacturing for large structural components made from Ti-6Al-4V. Conventional manufacturing routes as for example in the aerospace industry come along with up to 95% of waste material that has to be machined from the bulk material. LMD is an additive manufacturing process building parts based on a nozzle-fed powder by laser solidification. This technology offers unique advantages for the production of near net-shape parts. In contrast to the powder bed-based technologies it also provides a higher productivity rate.

Today LMD lacks reproducible process strategies manufacturing large parts in narrow tolerances and predictable residual stress states. Although Ti-6Al-4V is one of the most widely used materials in additive manufacturing with LMD, the occurrence of residual stresses is still a common cause for failure of parts or even the entire build job.

To reduce this effort, in this paper first the actual state of the anisotropic residual stress states is investigated for LMD-manufactured parts to obtain thorough knowledge of the process and shape-related dependencies with the quality aims. Based on these results an in-depth study for the influence of different exposure patterns on the residual stresses is shown. A simulation-based approach is chosen to develop a strategy for further optimization of the exposure. For validation, Crack Compliance Method has successfully been used in first experiments to determine the local distribution of residual stresses for several geometries - consecutively leading to a higher effort in the manufacturing-process development for such parts.

The gathered knowledge is applied to an 2.5 D prototype application and a 3 D complex hybrid aerospace application.

Keywords: laser metal deposition; residual stresses; crack compliance method; geometrical accuracy; anisotropic properties; titanium

---

\* E-mail address: mauritz.moeller@tuhh.de .

## 1. Introduction

An increase in usage of Titanium (Ti) content is witnessed in aviation industry, which accounts for 40% of the total titanium production owing to its good strength-to-weight ratio [1]. Conventional manufacturing techniques of Ti components in aerospace industry generate a waste of material as high as 95%. Laser Metal Deposition (LMD) is an additive manufacturing process that allows one to fabricate bulk materials with very high deposition rates compared to other AM techniques. It is a layered deposition welding technique in which atomized powder fed through a nozzle undergoes a sequence of melting and solidification process under the influence of laser beam, to form three-dimensional components [2]. LMD followed by milling process offers an efficient, resource conserving manufacturing method for large structural components made of Ti alloys like Ti-6Al-4V.

Despite of various research works, LMD still lacks reproducible process parameters and strategies to manufacture usable parts in narrow tolerances with predictable microstructural properties [3,4]. The building height of a single layer and the geometrical shape of the 3D component alter progressively with increasing part dimension and complexity, ultimately leading to increased post-processing efforts [5–7].

## 2. System Setup and Methodology

The used system setup consists of a 6kW Trumpf TruDisk 6001 multi-mode continuous wave disk laser with a wavelength of  $1.03\text{ }\mu\text{m}$ . A co-axial nozzle attached to the laser deposition head delivers atomized metal powder fed through a rotational table feeder. Because of high reactivity of Ti above  $800^{\circ}\text{C}$ , an inert gas (argon) atmosphere with less than 50 ppm of residual oxygen is ensured inside the self-fabricated building chamber, as shown in figure 1. The used Ti-6Al-4V powder is spherical with diameter ranging between 80 and  $150\text{ }\mu\text{m}$ .

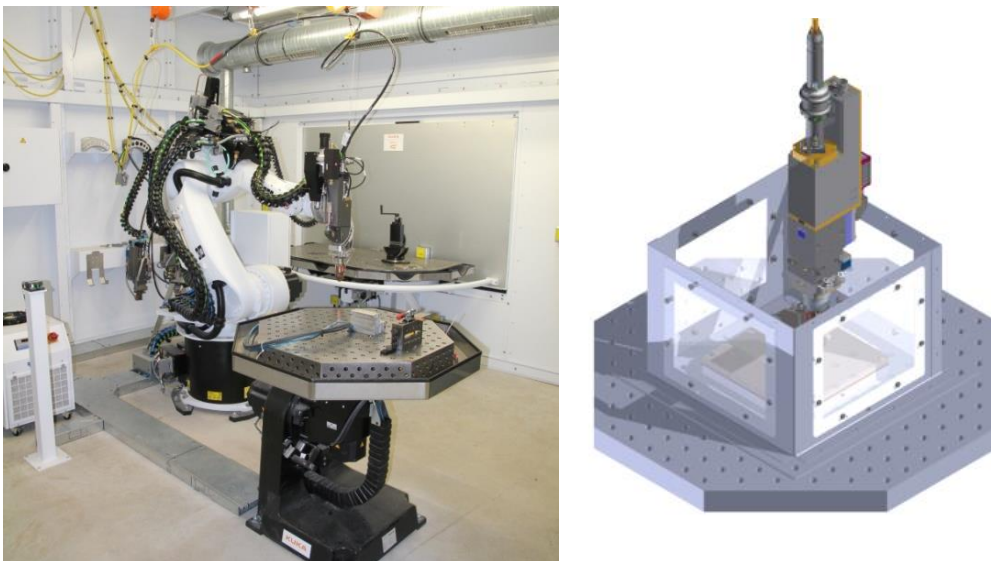


Fig. 1. (left) Robot cell (TruLaser Robot), (right) Shielding cabin for argon atmosphere

A generic process chain suitable for LMD process is developed to carry out the experimental investigations in a scientific approach. Figure 2 depicts pictorially the four major LMD phases. Conceptualization of the part begins from the result of topology optimization and consideration of certain manufacturing limitations. A CAD model is designed and the workpiece is divided into several weldable workpiece sections. These sections are then sliced depending upon the decided process strategy, part complexity and orientation in the base plate. LMD components are built by traversing the laser deposition head through a pre-determined vector path. Next step in the process chain is the path planning through robot programming of vector paths, followed by the final manufacturing phase.

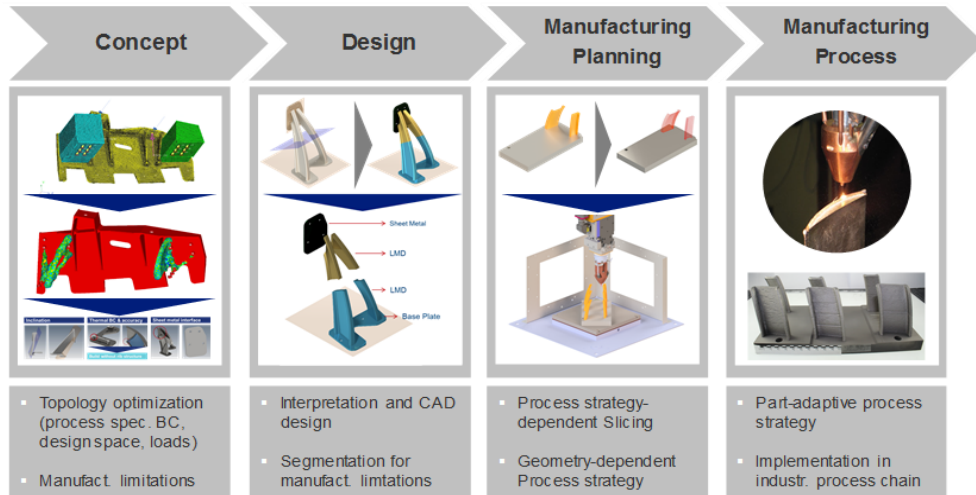
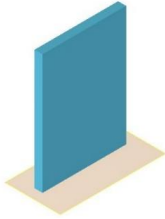
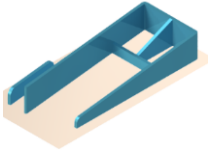



Fig. 2. Adapted manufacturing process chain for LMD

For this study, three components were designed in the increasing order of shape complexity, which were then manufactured following the above proposed process chain. Table 1 shows the CAD model of the three components along with the overall dimensions.

Table 1. 3D CAD model of different components with LMD built part photograph

Component	1	2	3
Shape Complexity	Low	Medium	High
CAD Model			
Overall Dimensions, in mm	70 x 4.5 x 68	210 x 95 x 35	100 x 80 x 70

### 3. Quality Targets

Initial investigations were carried out on component 1 to determine certain quality parameters like surface roughness, hardness, chemical composition, grain size and microstructure [8]. This study is extended to determine the dependence of geometry related quality targets with respect to shape complexity and process strategies. Hence, surface roughness and geometrical tolerance measurements are discussed in detail.

#### 3.1. Geometrical Tolerance

The capability of LMD process to build walls with narrow tolerance range has been proved by earlier research work [9]. Different building strategies were also examined to build inclined walls. The present study extends the research work to more complex part geometries. Initial LMD build trials were carried out with previously determined optimum process parameters of laser power, powder feed rate and transverse velocity. Figure 3 shows the photographs of the build components. Though component 1 is in close tolerance to designed specifications, considerable geometrical deviation is noted in component 2 and 3, especially at hot-spots like corners and T-junction, marked with red circle in figure 4. All three components are characterized with thinner wall thickness at the bottom layers and an increasing wall thickness as the build process progresses and once again decreasing thickness in the top-most layers. This three-phase model was identified in the previous research work, which persists also in the complex part geometries. Various closed loop process control techniques and building strategies have been proposed to overcome this undesirable effect [5–7,10].

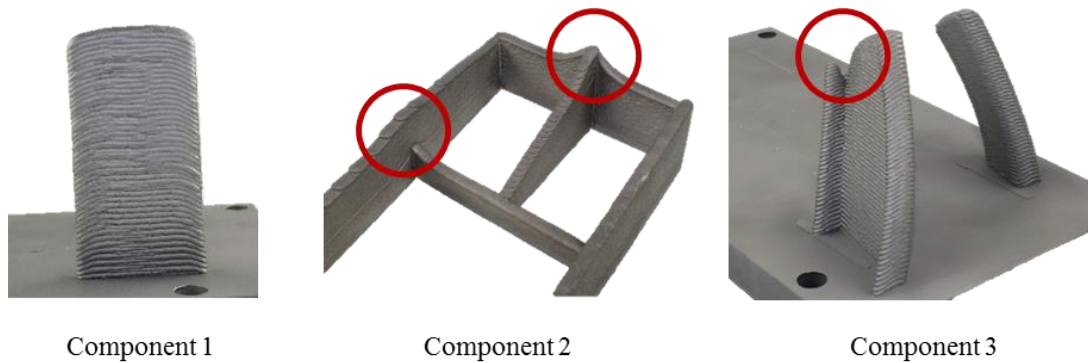


Fig. 3. LMD build components (without process optimization)

With increasing part complexity, it is evident that build quality is dependent not only on optimized process parameters but also other influencing factors. This paper continues to determine the influence of path planning strategies and various part building strategies on achievable geometrical tolerance.

### **Measurement technique**

For the determination of dimensional accuracy, the components were measured using a Coordinate Measuring Machine (CMM). WENZEL Präzision GmbH's mid-sized LH87 attached with a Renishaw PH10M motorized probe head was used along with a tactile probe and a 3D line scanner. The scanning process generates a point cloud represented by x, y and z coordinates at a rate of 48,000 points per second with an accuracy of 20 $\mu$ m. Component 1 was measured using the tactile probe and Component 2 and 3 were scanned using the line scanner to generate a point cloud. The point cloud was then compared with respective 3D CAD model using the PointMaster 5.0 software, resulting in a 3D geometrical deviation plot.

### **3.2. Residual stresses**

Residual stresses are characterized for being equilibrium state in even at the absence of external forces. These stresses can be classified by their formation caused by thermal or mechanical processing methods, by the distance they compensate to equilibrium or corresponding to the used measurement method [15], [22]. In this paper the classification of residual stresses on the particular compensation distance is applied (tab. 2).

The mechanical properties of a body are mainly influenced by the macro stresses. Especially when considering the conversion of residual stresses into plastic deformation, influence of the micro- and the sub micro stresses is negligible [15].

Table 2. Classification of residual stresses according to compensation distances (based on [19])

Classification	Dimension	Compensation distance	Formation
type I	macro stresses	The residual stresses compensate over long distances to equilibrium, often in the components dimension.	large temperature gradients, plastic deformation
type II	micro stresses	The stresses of the type II are balanced within the dimension of a grain.	multiphase materials, phase transitions
type III	sub micro stresses	Sub grain areas down to atomic distances compensate with this stress type.	interfacial surfaces, stress fields of dislocations

As long as the residual stresses are in self-equilibrium, there is no influence on the structure except that the residual stresses add up with potential external forces, which can be either negative or positive. However, once the yield strength is exceeded by the loads, plastic deformation occurs and in case of progressive deformation leads to cracking.

This local energy input leads to residual stresses, which can cause deformation or part failure during or even after the manufacturing for example in post processing steps. In this paper, a combination of experimental and numerical approaches is chosen to get an insight into the residual stress state of the manufactured part.

### 3.3. Numerical approach to determination of residual stresses

The heat effect of welding processes results in unwanted deformations of the processed parts. Distortions affect the manufacturing tolerances as well as decrease the quality of the built part. Predicting residual stresses and the resulting distortions is the core objective of the structural welding simulation [18]. The basis for the calculation of distortions is the determination of the temperature field. The structure temperature field is a numerical abstraction of the real temperature field and thus requires calibration by empirical experiments.

The welding structure simulation is based on the heat conduction model and the heat input during welding operations [20]. For the following field equation of heat conduction an isotropic, homogeneous heat conduction model is assumed as well as a heat input by a volumetric heat source [17],[20].

$$\frac{\partial T}{\partial t} = \frac{\lambda}{c_p} \left( \frac{\partial^2 T}{\partial x^2} + \frac{\partial^2 T}{\partial y^2} + \frac{\partial^2 T}{\partial z^2} \right) + \frac{1}{c_p} \frac{\partial Q_{vol}}{\partial t} \quad (1)$$

In addition to the definition of the heat supply, boundary conditions for the different heat flows at the borders between component and environment have to be determined. Thermodynamic constraints can be split in convective, radiation and conductive heat flows [11],[18].

Welding structure simulation is set in the software *Simufact.welding*, while the meshing is conducted in *Altair Hypermesh* choosing eight node brick elements. To apply an optimized element size with minimal error, a convergence study for different element sizes is conducted (0.05 mm to 5 mm) a based on this study differing element lengths in the range from 0.25 mm to 2 mm are used. The region of interest, the weld, is

discretized with finer elements, while with increasing distance from the weld, element size is gradually increased to reduce the computation time. Furthermore, the computation cost is decreased on one hand by using a symmetry plane on the center line of the weld and on the other hand by adding new elements during the transient computation (Fig. 4 (a)).

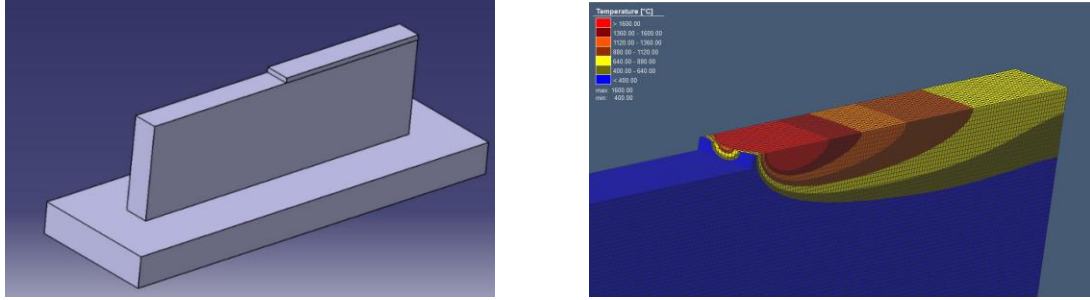


Fig. 4. (a) Geometrical model for simultaneous creation of layer elements, (b) formation of temperature field in 32 layer

In order to identify the heat input during the LMD process, a simplified experimental set-up is designed (Fig. 6). An additively built wall is milled (width: 50 mm, height: 30 mm, thickness: 4 mm) as the sample for validation. The wall is arranged in the shielding cabin in a way, that the perspective of a IR camera (IRCam Equus 81kM MCT) is perpendicularly to the front face of the wall to measure the temperature field. On the other side of the sample, discrete temperature measurement is conducted with thermocouples (type K, diameter: 0.25 mm). Positions of the thermocouples from the top are 1 mm, 4 mm, 7 mm and 10 mm (placed at 5 mm and 25 mm from the left edge).

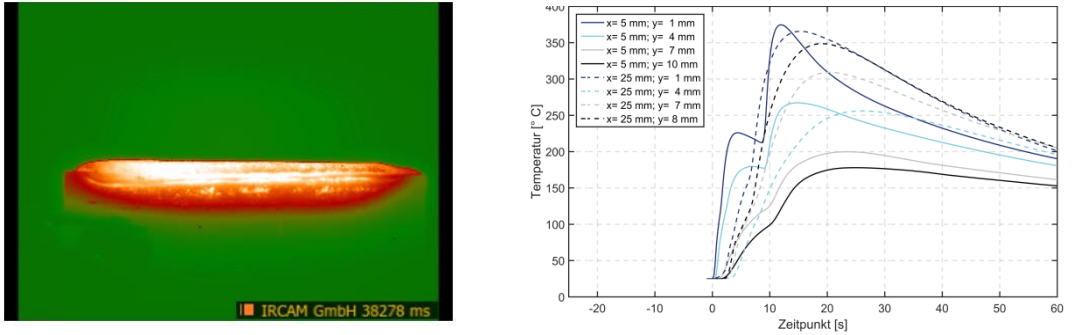


Fig. 5. (a) Temperature field after 12 s (camera system works at a spectral range of 3-5  $\mu\text{m}$  and with a resolution of 256 rows and 320 columns.), (b) Temperature time curves from thermocouples in validation experiment

The IR camera is calibrated using temperature feedback from the thermocouples, while the relationship between the measured counts  $C(T)$  and the corresponding surface temperature  $T$  is described by a modified Stefan Boltzmann equation (Fig 5 (a)):

$$C(T) = a * (T + 273,15K)^4 + b \quad (2)$$

The two fitting parameters  $a$  and  $b$  are adjusted to fit the calibration curve to the measured surface temperature during the calibration process. Fig. 5 (a). shows the measured temperature field for validation experiments (taken 12 s after deposition start) as well as the temperature curves used for camera calibration is shown in Fig. 5 (b). The measured temperatures – discrete and temperature field- are used for calibration of the simulated heat input. Final residual stresses are recorded after 20 s duration of cooling along the slot plane in the simulation model. The results are compared to the measured residual stresses in Crack Compliance Method.



Fig. 6. Experimental set-up for empirical validation of numerical heat input

### 3.4. Experimental determination of residual stresses

Cheng and Finnie (1985) developed the technique of determining residual stresses by controlled relaxation using successive extension of a slot (Fig. 7) [12]. The slot is continuously increased in increments in one direction in which the residual stresses should be identified. Today, manufacturing methods are available which just remove small amounts of materials for the slot generation, so that the stress state is only affected slightly and negligibly as additional residual stresses are introduced [19]. Under a global elastic stress field the slot can be regarded as a crack, so that for the calculation of the causal stresses from the measured strains there are linear-elastic fracture mechanics applicable. The strain shift for the current slot progress can be calculated with [21]:

$$K_{Irs}(a) = \frac{E'}{Z(a)} \frac{d\varepsilon_m}{da} \quad (3)$$

The stress intensity factor depends on the residual stress state before the slot is conducted [21]:

$$K_{Irs}(a) = \int_0^a h(x, a) \sigma_{rs}(x) dx \quad (4)$$

Assuming a known stress intensity factor, the inversion of (7) can be used to calculate  $\sigma_{rs}$ .

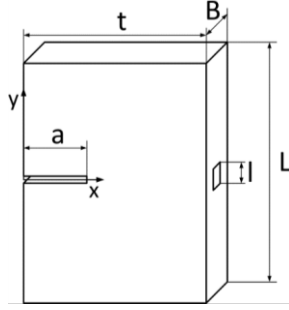


Fig. 7. Specimen for Crack compliance analysis according to [13] [14]

In contrast to the above mentioned incremental stress method, the present work solves this inverse mechanics problem using a series expansion assumption for the residual stress determination [13],[16]:

$$\sigma_{yy}(x) = \sum_{j=2}^m A_j P_j(x) \quad (5)$$

with  $C_{ij} = \varepsilon(a_i)|_{\sigma_{inp}=P_j(x)}$  using elastic superposition principle

$$\Leftrightarrow \varepsilon(a_i) = \left( \sum_{j=2}^m C_{ij} A_j \right) E \quad (6)$$

The unknown amplitudes has to be determined from the measured strain, while the Legendre polynomials are chosen between 2 and 12 according to [14]. The inverse of (9) and the application of matrix formulation leads to the calculation of the amplitude vector:

$$A = E [(C^T C)^{-1} C^T] \varepsilon_{meas} \quad (7)$$

Lee and Hill (2006) propose an approach for the determination of compliance matrices for variable quad geometries. If a set of requirements for the prism is fulfilled, the compliances can be calculated using:

$$C\left(\frac{a}{t}, P_n\right) = \sum_{k=1}^{15} b_{n,k} \left(\frac{a}{t}\right)^k = b_{n,1} \left(\frac{a}{t}\right) + b_{n,2} \left(\frac{a}{t}\right)^2 + \dots + b_{n,14} \left(\frac{a}{t}\right)^{14} + b_{n,15} \left(\frac{a}{t}\right)^{15} \quad (8)$$

In the present paper wire-electric discharge machining (WEDM) is used for cutting the slot in 28 discrete steps with a length of 1 mm each (Fig. 8).

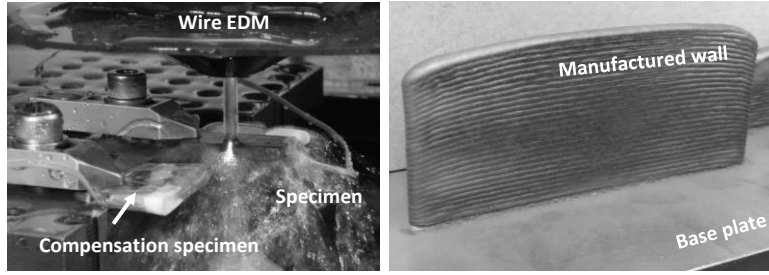


Fig. 8. (a) discrete slot expansion using wire EDM , (b) shielding cabin for argon atmosphere

The strain gages are set in half bridge configuration. The first strain gage is positioned at the back face of the specimen and the second one is used for temperature compensation ( $k$ -factor = 1.98, resistance =  $120\ \Omega$ , grid length = 1.5 mm). The dimensions of the specimen are  $t = 34\text{ mm}$ ,  $B = 4.5\text{ mm}$ ,  $L = 70\text{ mm}$ , specific strain gage length ( $l/t$ ) = 0.04412,  $0\text{ mm} < a < 28\text{ mm}$ ,  $s = 0$  and  $E = E' = 114\text{ GPA}$  ( $B/t < 0.5$ ).

#### 4. Results

Geometrical deviation plot of component 2 is shown in figure 9. Component 2 built with path planning strategies shows a tolerance value 33% lesser than the one built without any process optimizing strategy. This confirms the highly influential effect of process strategy over geometrical accuracy.

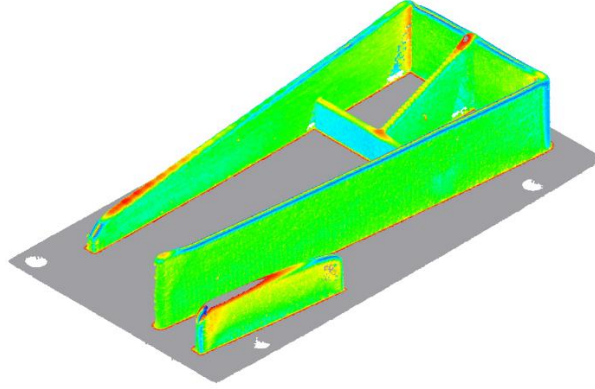
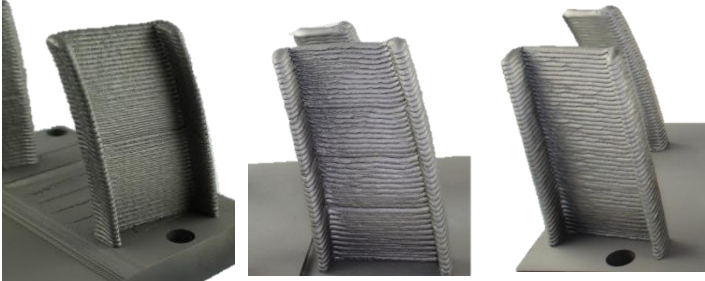


Fig. 9. 3D geometrical deviation plot of component 2

A comparison between different building strategies of component 3 is tabulated in table 3. The building process involves both weld and non-weld motions of the deposition head. Therefore, productivity for the LMD process is defined by the ratio of weld time to total time.

Table 3. Comparison of different building strategies for Component 3

Building strategy	1	2	3
LMD part			
Nominal weld width, mm	4.0	5.0	5.0
Build Time, mm:ss	23:45	17:15	16:05
Productivity	67%	92%	99%
Standard deviation, mm	0.3737	0.5620	0.4092
Tolerance (90% C.I.), mm	$\pm 0.6128$	$\pm 0.9200$	$\pm 0.6700$
Tolerance (95% C.I.), mm	$\pm 0.7474$	$\pm 1.124$	$\pm 0.8184$

It is observed that geometrical accuracy could be controlled using appropriate building strategy. Building strategy 1 has the least tolerance range, but also has the least productivity. There is a significant reduction in nominal wall thickness when adopting strategy 1, because of more available cooling time between consecutive layers. Hence, cooling time is another influential process parameter that affects part quality. Components with a maximum of 35° inclination are manufacturable using the present system setup and process strategy. Further investigations are required in identification of other influential factors and development of building strategies to manufacture freeform complex components with more inclination angle in narrow tolerances.

## 5. Conclusion

Based on various experimental investigations, it is evident that geometrical tolerance increases with part complexity. Additional process strategies are essential along with optimum process parameters for fabricating components with increasing part complexity. Appropriate path planning strategy can result in narrow tolerance deviation. Part building strategies has an influence not only on quality of the LMD built part, but also impacts cost and productivity.

## REFERENCES

- [1] Kristy Chi, "A look at Global Metallic Fastener Development in Two Airline Manufacturing Giants, Boeing and Airbus," *Industry Focus*, pp. 178–182.
- [2] G. Buchfink, *The laser as a tool: A light beam conquers industrial production*, Vogel, Würzburg, 2007.
- [3] T. Liencke, G. A. Adam, S. Leuders et al., "Systematical determination of tolerances for additive manufacturing by measuring linear dimensions," in *26 th Annual International Solid Freeform Fabrication Symposium*, Austin, 2015.
- [4] R. Cottam and M. Brandt, "Laser Cladding of Ti-6Al-4V Powder on Ti-6Al-4V Substrate: Effect of Laser Cladding Parameters on Microstructure," *Physics Procedia*, vol. 12, pp. 323–329, 2011.
- [5] A. Fathi, A. Khajepour, E. Toyserkani et al., "Clad height control in laser solid freeform fabrication using a feedforward PID controller," *The International Journal of Advanced Manufacturing Technology*, vol. 35, 3-4, pp. 280–292, 2007.
- [6] L. Tang and R. G. Landers, "Layer-to-Layer Height Control for Laser Metal Deposition Process," *Journal of Manufacturing Science and Engineering*, vol. 133, no. 2, p. 21009, 2011.
- [7] E. Fearon and K. G. Watkins, *Optimisation Of Layer Height Control In Direct Laser Deposition*, Laser Institute of America, Orlando, Fla., 2004.
- [8] Möller, M., Ewald, A., Weber, J., Heilemann, M., Herzog, D., Emmelmann, C., "Characterization of the Anisotropic Properties for Laser Metal Deposited Ti-6Al-4V," *Journal of Laser Applications*, 2016.
- [9] M. Möller, N. Baramsky, A. Ewald et al., "Evolutionary-based Design and Control of Geometry Aims for AMD-manufacturing of Ti-6Al-4V Parts," *Physics Procedia*, vol. 83, pp. 733–742, 2016.
- [10] D. Hu and R. Kovacevic, "Sensing, modeling and control for laser-based additive manufacturing," *International Journal of Machine Tools and Manufacture*, vol. 43, no. 1, pp. 51–60, 2003
- [11] Bathe, K.; Zimmermann, P: *Finite-Elemente-Methode*. (2002), Springer
- [12] Cheng, W., Finnie, I.: A method for measurement of axisymmetric axial residual stress in circumferentially welded thin walled cylinders. In: *Journal Engineering Material Technology*., Vol.107, (1985) pp.181-185
- [13] Cheng, W., Finnie, I.: A summary of past contributions on residual stresses. (2002), Vols. 404-407, pp.509-514
- [14] Lee, M.; Hill, M.: Effect of strain gage length when determining residual stress by slitting. In: *Journal of Engineering Materials and Technology* 129 (2006), pp. 143-150
- [15] Mercelis, P. ; Kruth, J.-P.: Residual stresses in selective laser sintering and selective laser melting. In: *Rapid Prototyping Journal* 12 (2006), pp. 254–265
- [16] Prime, M.: Residual stress measurement by successive extension of a slot: The crack compliance method. (1999), *Applied mechanics review* 52, pp. 75-96
- [17] Radaj, D.: *Wärmewirkungen des Schweißens: Temperaturfeld, Eigenspannungen, Verzug*. (1988), Springer
- [18] Radaj, D.: *Eigenspannungen und Verzug beim Schweißen: Rechen- und Meßverfahren*. (2002), DVS-Verlag
- [19] Rossini, N.; Dassisi, M.; Benyounis, K., Olabi, A.: Methods of measuring residual stresses in components. In: *Materials and Design* 35 (2012), pp. 572-588
- [20] Rykalin, N.: *Berechnung der Wärmevergänge beim Schweißen*. (1957) VEB Verlag
- [21] Schindler, H. J.: Determination of residual stress distributions from measured stress intensity factors., In: *International Journal of fracture* 74 (1995), R23-R30
- [22] Withers, P. J. ; Bhadeshia, H. K. D. H.: Residual Stress - Measurement Techniques. In: *Material Science and Technology* 17 (2001), pp. 355–365